Multidirectionally distributed feedback photonic crystal lasers

Masahiro Imada,[1,2,*] Alongkarn Chutinan,[1,2] Susumu Noda,[1,2,†] and Masamitsu Mochizuki[1,2]

[1]*Department of Electronic Science and Engineering, Kyoto University, Yoshida-honmachi, Sakyo-ku, Kyoto 606-8501, Japan*

[2]*Core Research for Evolutional Science and Technology, Japan Science and Technology Corporation, Kyoto 606-8501, Japan*

The lasing mode of a two-dimensional (2D) photonic crystal laser with in-plane multidirectionally distributed feedback effect is analyzed theoretically and experimentally. From an investigation of the Bragg diffraction conditions at several points in the photonic band diagram where lasing is expected, we identify a particular Γ point at which lasing occurs due to the coupling of lightwaves propagating in six equivalent Γ-X directions and diffraction normal to the substrate surface. In order to investigate the lasing mode in detail, the distribution of the electromagnetic field at the band edges at the Γ point is calculated, and each band edge is found to have a different field pattern. The lasing characteristics of the 2D photonic crystal laser at the lasing wavelength corresponding to the Γ point are measured. Single-mode lasing over a broad circular area is observed by microelectroluminescence measurements under pulsed conditions at room temperature. We also demonstrate the correspondence between the measured lasing wavelengths and calculated band edges by comparing the polarization characteristics with the calculated distribution of the electromagnetic field. The results indicate that 2D coherent lasing oscillation does, in fact, occur due to the multidirectional coupling effect in the 2D photonic crystal. From the theoretical calculation, we show that the polarization patterns of the lasers can be controlled by introducing artificial lattice defects.

I. INTRODUCTION

The semiconductor laser plays an important role in the modern information society. Although it is desirable that devices have only one lasing wavelength or one lasing mode, in practical devices, the number of modes inside a laser cavity is proportional to the size of the laser cavity. To control the number of modes, a mechanism called distributed feedback[1,2] (DFB) has been widely utilized in commercial semiconductor lasers. A grating or one-dimensional periodic structure embedded in the DFB laser induces Bragg diffraction, resulting in coupling between two waves propagating in the forward and backward directions. This coupling effectively amplifies those modes with wave vectors satisfying the Bragg condition. Recently, lasers based on two-dimensional (2D) photonic crystals or 2D periodic structures have been reported.[3–6] Due to the two dimensionality of such devices, the Bragg diffraction that occurs is multidirectional. This is physically very interesting because multidirectional Bragg diffraction may be able to yield coupling mechanisms unattainable using traditional DFB lasers, possibly leading to control of the lasing mode over a large 2D area. From the viewpoint of engineering, such control of the lasing mode may have various important applications such as high-power lasers or surface-emitting lasers with very narrow divergence angles.

Previously, we reported room temperature lasing in a 2D photonic crystal surface-emitting laser.[3] However, the characteristics of the device have yet to be theoretically or experimentally investigated in detail. For example, the correspondence between the measured lasing characteristics and the calculated lasing mode in 2D photonic crystal remains unclear. In this work, we present detailed theoretical analyses and experimental results for 2D photonic crystal lasers. In Sec. II, we describe the theoretical results for the lasing mode in the 2D photonic crystal cavity. In Sec. III, we describe the experimentally observed lasing characteristics of the device in detail and discuss the correspondence between the measured results and the calculated lasing mode.

II. THEORETICAL ANALYSIS OF LASING MODE IN 2D TRIANGULAR-LATTICE STRUCTURE

A. Calculation of band diagram by 2D plane-wave expansion method

In this section, we analyze the lasing mode in the 2D triangular-lattice structure. Figure 1(a) shows a schematic and reciprocal lattice of a 2D photonic crystal with a triangular lattice. The two arrows in the left side figure indicate the two specific directions Γ-X and Γ-J. First, we calculate the dispersion relation or the band diagram of the modes in our device. We employ the 2D plane-wave (PW) expansion method[7] to calculate the band diagram because the device structure is two dimensionally periodic. However, the 2D PW expansion method assumes an infinite length in the third dimension, which is not the case in the actual device. To compensate for this, we consider the fact that in the actual device, the majority of light is confined within the active layer, and only a small fraction of light is distributed in the 2D photonic crystal layer.[3] The calculable effect of the 2D photonic crystal will be smaller than that in an infinite structure, or more specifically, the effect will be proportional to the fraction of light confined within the 2D photonic crystal layer. To account for this, we must determine two parameters for 2D PW calculation; the dielectric constant for the circular rod (ε_a) and the background (ε_b).

These two dielectric constants are derived by calculating the distribution of the electric field in the vertical direction of the device by the transfer-matrix method. The calculated result is shown in Fig. 1(b). From the calculated result, we
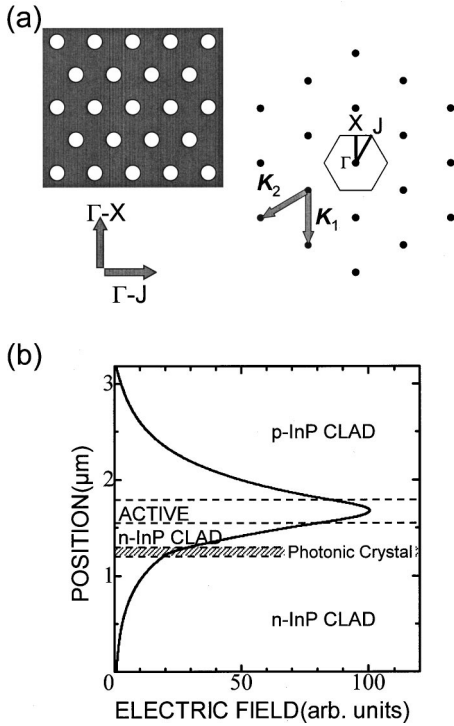
65 195306-1

FIG. 1. (a) Schematic and reciprocal lattice of a 2D photonic crystal. Two arrows in the left side indicate two particular directions Γ-X and Γ-J. K_1 and K_2 in the right side figure indicate the grating Bragg vectors of the structure. (b) Distribution of electric field in the vertical direction of the device calculated by transfer-matrix method. The hatched area corresponds to the 2D photonic crystal layer.

estimate the effective refractive index n_{eff} of the fundamental mode and the fraction of the electric field within the photonic crystal layer, giving the confinement factor for the photonic crystal layer. The estimated values are 3.26 and 1.26%, respectively.

Next, we determine ε_a and ε_b using two conditions; (1) the average dielectric constant $[=f\varepsilon_a+(1-f)\varepsilon_b; f$ is a filling factor] is equal to n_{eff}^2, and (2) the difference $\Delta\varepsilon=\varepsilon_b-\varepsilon_a$ is equal to 1.26% of the difference between the dielectric constant of In P$(=10.5625)$ and air (the two materials composing the photonic crystal layer). Using the filling factor of 0.2 for the fabricated device described in the Sec. III, we obtain $\varepsilon_a=10.5625$ and $\varepsilon_b=10.6834$. Finally, we use the 2D PW expansion and ε_a and ε_b to calculate the band diagram. The result is shown in Fig. 2(a), and will be discussed in Sec. II B. A total of 331 plane waves were used in this calculation.

We verified the validity of the above approximation by using the same method to calculate the band gap (stop band) of a 1D DFB laser. The calculated results agreed with the measured results and the results calculated by conventional theoretical analysis of a 1D DFB laser.

B. Bragg diffraction in 2D triangular-lattice structure

Figure 2(a) shows the calculated band diagram of the structure for transverse-electric (TE) mode. It is expected
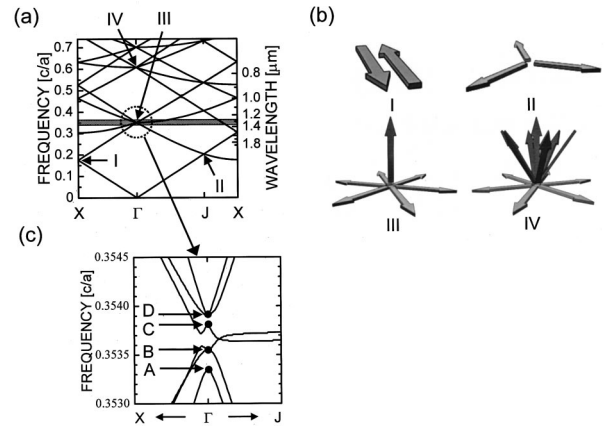

FIG. 2. (a) Dispersion relation or band diagram of electromagnetic waves propagating in a 2D photonic crystal. (b) Schematic showing propagating directions of coupled waves at points I–IV. (c) Enlarged band diagram showing the vicinity of point III.

that lasing occurs at specific points on the Brillouin-zone boundary and at the points at which bands cross and split. At these lasing points, waves propagating in different directions couple, significantly increasing the mode density. It is particularly interesting that each of these points exhibits a different type of wave coupling according to the Bragg conditions (see the Appendix). For example, point I corresponds to the coupling of only two waves, those propagating in the forward and backward directions, as shown in Fig. 2(b). This coupling is similar to that of a conventional DFB laser. However, as there are six equivalent Γ-X directions in the structure, a cavity can exist independently in each of the three different directions, forming three independent lasers. Point II has a unique coupling characteristic unachievable in conventional DFB lasers, the coupling of waves propagating in three different directions.[8] The Γ-J direction also exists in each of the six directions, therefore, two different lasing cavities in different Γ-J directions coexist independently. The applicability of this mode is uncertain because the laser light is emitted in the three different directions. Point III corresponds to coupling of waves propagating in six different directions. This appears to be a good choice of mode because it includes in-plane coupling in all six directions; $0°$, $\pm60°$, $\pm120°$, and $180°$. In addition, the coupled light is emitted perpendicular from the surface according to first order Bragg diffraction, as described in the Appendix. This is the same phenomenon that occurs in conventional grating-coupled surface-emitting lasers, and facilitates the extraction of light from the device.[9] There are many other points at frequencies higher than point III where waves are multidirectionally coupled in plane and out of plane. However, the angles of out-of-plane coupling by Bragg diffraction either vary from $90°$ entirely or have a component that varies from $90°$, i.e., light is also coupled out of plane at an angle other than $90°$. For example, at point IV, light is coupled out of plane at an angle of $54.7°$ (diffraction to air) as well as at $90°$. Therefore, we consider that the point offering the most desirable characteristics is point III.
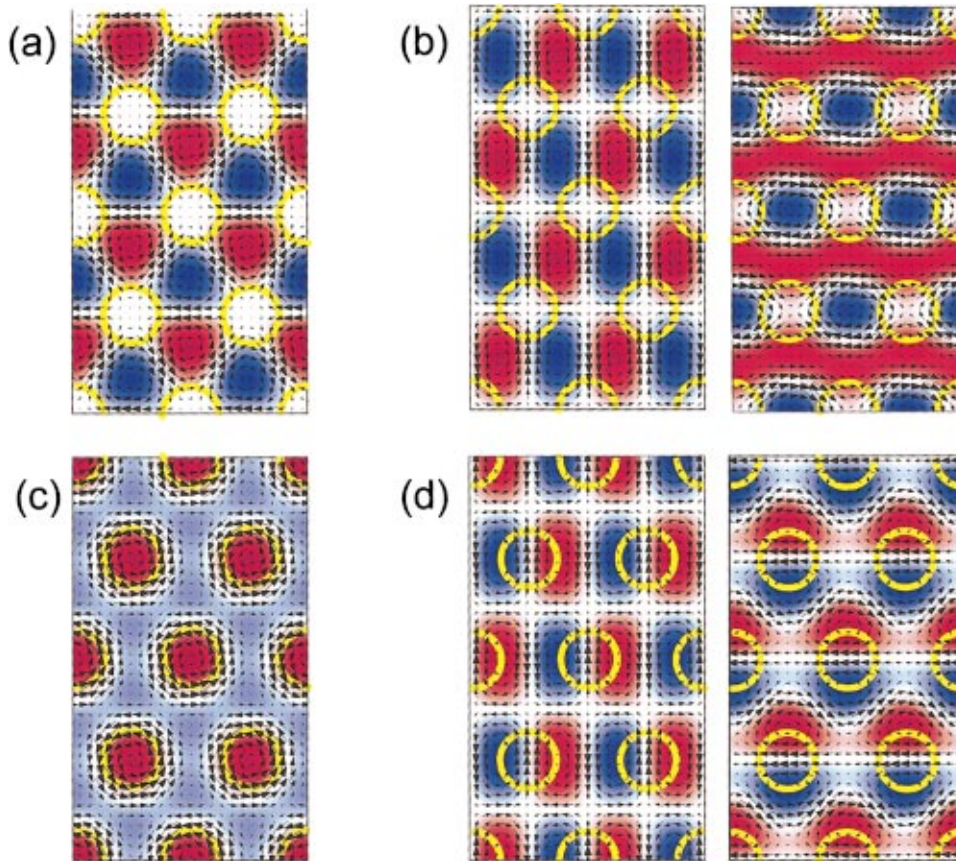
FIG. 3. (Color) Electromagnetic field distributions of six modes in bands $A-D$. Red and blue areas correspond to positive and negative magnetic fields perpendicular to the plane. Black arrows indicate in-plane electric-field vectors and yellow circles indicate lattice points. (a) Band A, hexapole mode. (b) Band B, pair of doubly degenerate quadrupole modes. (c) Band C, monopole mode. (d) Band D, pair of doubly degenerate dipole modes.

C. Lasing mode in 2D photonic crystal surface-emitting laser

The calculated band diagram in the vicinity of point III is shown in Fig. 2(c). There are six bands, resulting from the six coupling waves. At the Γ point, there are two pairs of doubly degenerate bands and two pairs of nondegenerate bands. We will call these bands A, B, C, and D, as indicated in Fig. 2(c); bands A and C are nondegenerate and bands B and D are doubly degenerate. The electromagnetic field distribution in the plane of the photonic crystal plane calculated for each mode by the plane-wave expansion method is shown in Fig. 3. Figures 3(a)–3(d) correspond to bands $A-D$, respectively. The amplitudes of magnetic fields in the direction perpendicular to the plane are indicated by the red and blue areas, corresponding to positive and negative amplitudes, respectively. The arrows indicate the electric-field vectors in the plane, and the yellow circles indicate the locations of lattice points. It can be clearly seen from the figure that the different modes are characterized by different magnetic patterns, which is useful for classifying the lasing modes according to group theory.[10] The magnetic field for band A is divided into three positive and three negative areas around each lattice point, referred to here as a hexapole mode. For band B, there are two positive and two negative areas around each lattice point, called a quadrupole mode. Bands C and D are characterized by monopole and dipole modes, respectively. The fabricated 2D photonic crystal lasers can be used in any of the four modes, with the corresponding polarization pattern.

D. Calculation of surface-emitting components of lasing mode

These results calculated by the 2D PW expansion represent in-plane electromagnetic (EM) fields. However, the property of interest observed experimentally is the surface-emitting component of these EM fields. These theoretical results can, therefore, not be compared directly to the experimental results. To make a valid comparison, we need to calculate the surface-emitting components of each lasing mode using a 3D method.

We employ the 3D finite-difference time-domain (FDTD) method[11,12] to calculate the surface-emitting components of the lasing mode. Figure 4 shows the model used for the 3D FDTD calculation. The 2D photonic crystal is formed from a dielectric slab with dielectric constant $\varepsilon_b=14$ and thickness 0.3 μm (or $0.6a$), containing circular rods with dielectric constant $\varepsilon_a=8$ and diameter 0.3 μm. The cladding layers above and below the slab are air. Mur's second-order absorbing boundary condition is employed. The photonic crystal is clearly finite in the third dimension, which opposes the infinite assumption in the 2D PW expansion calculations. The parameters used in the FDTD calculation are $\Delta x = \text{sqrt}(3)/16a$, $\Delta y = 1/10a$, $\Delta z = 1/10a$, and $\Delta t = 0.5\Delta y/c$, where c is the speed of light in a vacuum. EM fields are excited for each lasing mode at the center of the 2D photonic crystal, corresponding to the active region under an electrode. As the lasing mode is a Bloch wave, the excited dipoles are placed periodically at antinodes according to the polarization pattern of the appropriate mode, as shown in Fig. 3. The surface-emitting components of excited EM
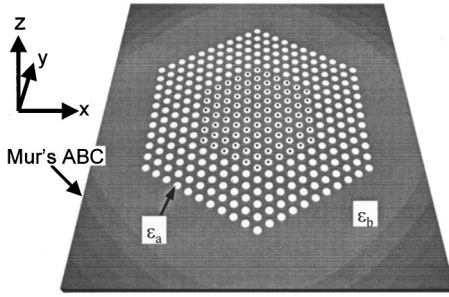
FIG. 4. Schematic of 2D photonic crystal slab consisting of two dielectric materials; a background ($\varepsilon_b = 14$) and circular rods ($\varepsilon_a = 8$). The slab thickness is $0.6a$. Solid points indicate dipole locations in FDTD calculation.

fields are observed in the plane parallel to the slab at a distance of 2.0 μm from the surface.

In contrast to the ε_a and ε_b of ~10.6 defined in the 2D PW expansion model, ε_b in the 3D FDTD model is set larger in order to confine most of the light within the slab in consideration of the thinness of the slab, and ε_a is set smaller so as to increase the contrast with ε_b and consequently the photonic crystal effect in order to save computational memory and time. The band structure used for the FDTD model is the same as that used for the 2D PW expansion calculation, except for shifted frequencies. The lasing modes can, therefore, be correlated between the two models. The points of interest are the lasing mode inside the 2D photonic crystal slab and leakage to the surface of the device. Although this model is not entirely accurate because we were unable to use an exact structural model due to limited computational resources, the model preserves the essential properties of the system and is considered to be sufficiently detailed.

III. MEASUREMENTS OF LASING CHARACTERISTICS AND COMPARISON WITH THEORETICAL CALCULATIONS

A. Fabrication and basic lasing characteristics

Figure 5(a) shows a schematic of the 2D photonic crystal laser reported previously.[3] The structure consists of two InP wafers, A and B. Wafer A has seven periodic structures of an InGaAsP ($\lambda_s = 1.36$ μm)/InGaAsP ($\lambda_g = 1.1$ μm) multiple-quantum-well (MQW) active layer that emits light at a wavelength of 1.3 μm. Wafer B is an n-InP substrate having a triangular-lattice 2D photonic crystal formed over a 480-μm-diameter circular area by electron-beam lithography (ELIONIX ELS-3700) and reactive ion etching (SAMCO RIE-10N). The 2D photonic crystal consists of air holes ($n = 1.0$) and InP ($n = 3.25$). The wafers are fused together by heating at 620 °C for 30 min in a hydrogen atmosphere. A circular electrode with a diameter of ~350 μm is formed over the region where the photonic crystal is embedded, leaving a ring of the device exposed for the surface emission. The lattice constant a is 0.462 μm, and the spontaneous emission wavelength of the MQW active layer coincides with the frequency of point III. Figure 5(b) shows the light output-current (L-I) characteristics of the device. We
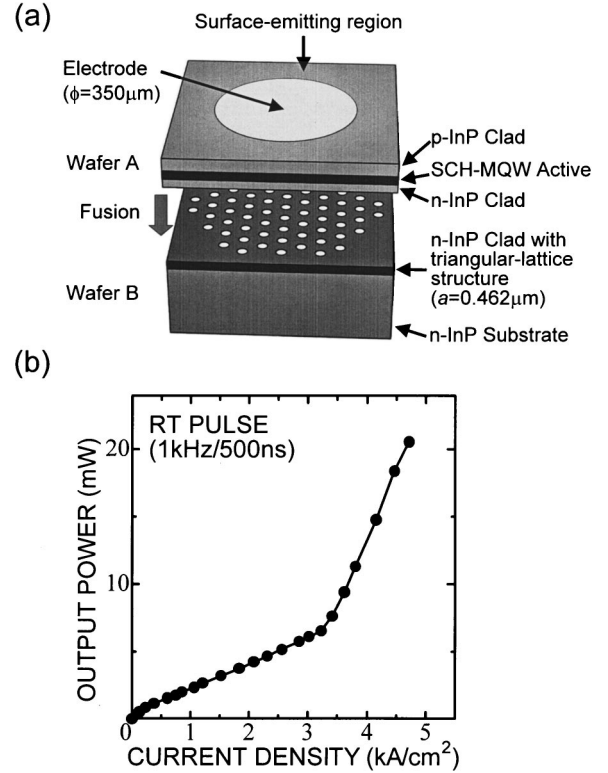

FIG. 5. (a) Schematic of 2D photonic crystal laser with triangular-lattice structure embedded by wafer fusion. (b) L-I characteristics of the device measured from the topside of the device.

achieved current injected lasing oscillation under pulsed conditions at room temperature with a maximum output power of greater than 20 mW. As described above, the light is also coupled perpendicularly out of plane by first-order Bragg diffraction, which facilitates the measurement of the various characteristics of the device from the top. Lasing oscillation was observed over a large area where the 2D photonic crystal was formed according to a near-field pattern (NFP) of the device (see Fig. 6 center) with a very narrow divergence angle (less than 1.8°, see Fig. 6).[3] The narrow divergence angle is due to the extensive 2D-area lasing oscillation of the device. The divergence angle $\Delta\theta$ of the Gaussian beam emitted from an area of radius R can be estimated by the following equation:

$$\Delta\theta = 2 \tan^{-1}[\lambda/(\pi R)],$$

where λ is the lasing wavelength (1.285 μm). Here, we assume a radius R of 32.5 μm, taken as an approximation of the area of the ring of width ~65 μm. The present device has a $\Delta\theta$ of 1.44° according to this calculation. These calculated results are considered to be consistent with the observed lasing mode. The difference between the measured and theoretical values is considered to be due to the fact that (1) the fabricated device has a ringlike beam spot, and (2) the beam does not have a Gaussian beam profile, rather, the beam profile decreases exponentially in a similar manner to conventional 1D grating-coupled surface-emitting lasers.[9]
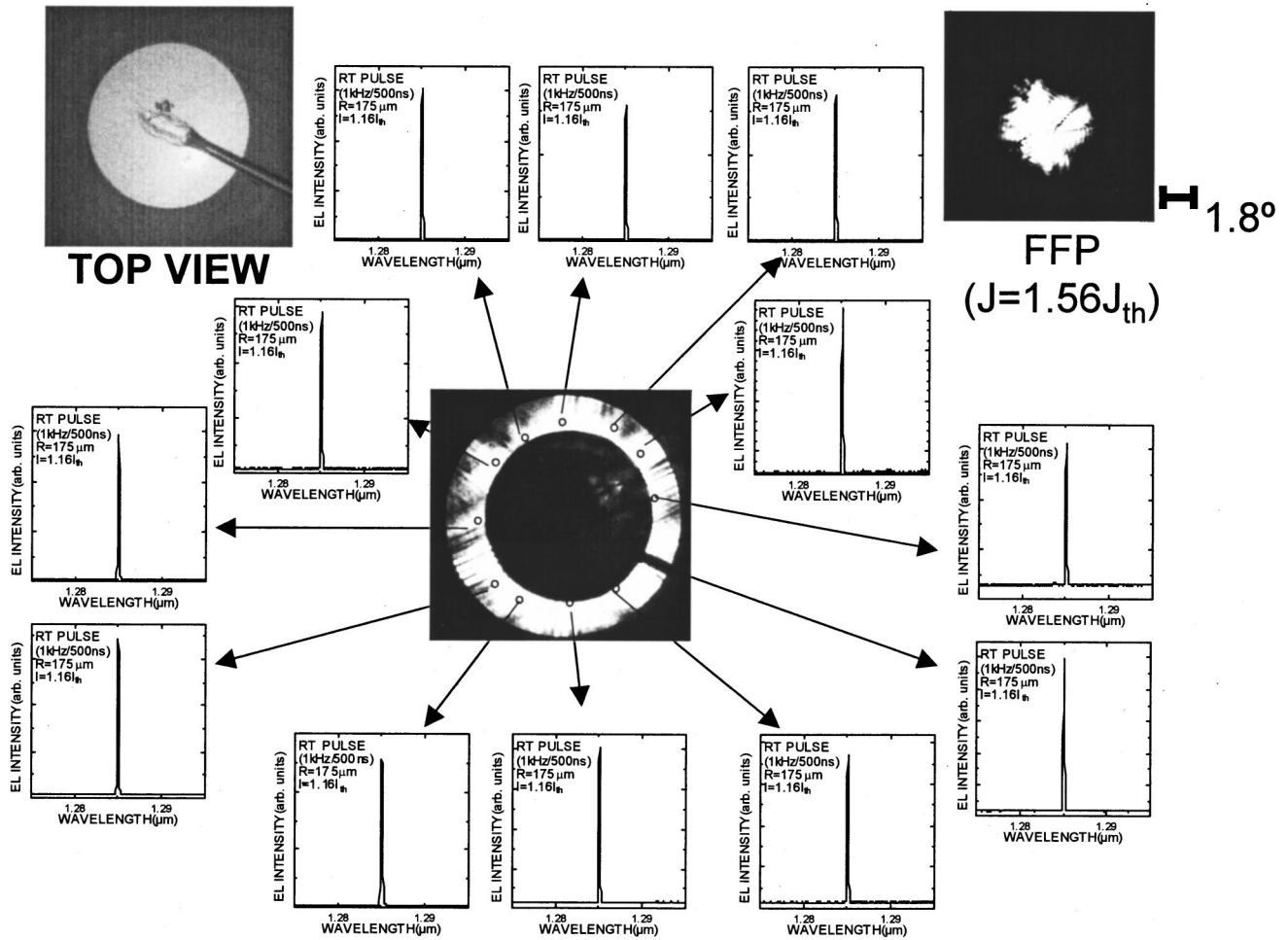
FIG. 6. Lasing spectra at various points on the lasing area as obtained by microelectroluminescence measurements. The near-field pattern of the device is shown at the center of the figure. Circles in the near-field pattern show the measurement points, each with diameter of about 15 μm. Top left: Top view of device showing the electrode and gold wire. Top right: Far-field pattern of the device.

B. Distribution of lasing wavelength and polarization characteristics of 2D photonic crystal laser

The lasing spectra was examined at different points over the lasing area by microelectroluminescence (MEL) measurements in order to confirm that lasing occurs at the same wavelength over the entire surface area. The results are shown in Fig. 6. The circles in the NFP indicated the measurement points; each point is about 15 μm in diameter. Lasing does indeed occur at the same wavelength at all measured points, despite the large area (diameter 480 μm). This is strong evidence that the lasing mode is singular and coherent over a large area, supporting the previous NFP and far-field pattern results (Fig. 6). We measured the lasing spectra of seven devices and found that the lasing wavelengths can be grouped into three bands, as shown in Fig. 7. Comparing this result with the calculated band diagram in Fig. 2(c), these groups appear to correspond to the band edges A, B, and D. The correspondence between the lasing wavelengths and the calculated band diagram was confirmed by investigating the polarization distribution for the A-band device (device No. 4) through MEL measurements. The results are shown in Fig. 8(a). The dark central area in the figure is the region covered by the electrode, and the three

white arrows indicate the three Γ-X directions. The hatched arrows indicate the direction of polarization at each measurement point. Each point in each Γ-X direction is polarized in the azimuthal direction, and each point between two Γ-X directions is polarized radially. The theory predicts that this lasing mode should resemble the hexapole mode shown in Fig. 3(a). However, as described in Sec. II D, Fig. 3(a) shows the field pattern inside the photonic crystal plane; the
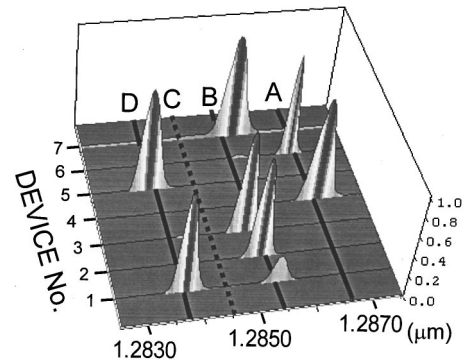

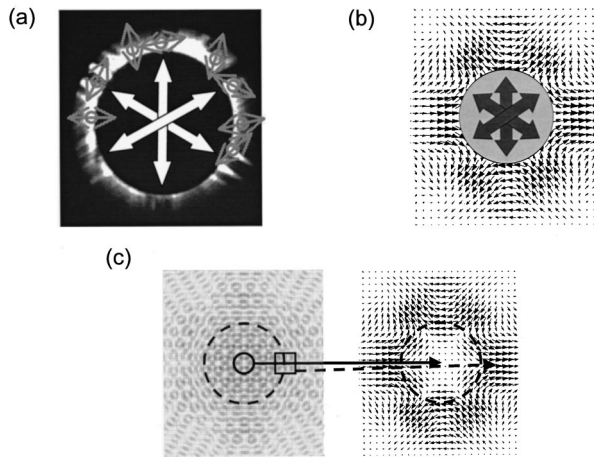FIG. 7. Lasing wavelengths of measured devices and corresponding lasing bands.

FIG. 8. (a) Polarization pattern of lasing mode of device No. 4. Dark central area is the region covered by the electrode. The three white arrows indicate each of the Γ-X directions, and the hatched arrows indicated the polarization direction. (b) Surface-emitting component of hexapole mode calculated by 3D FDTD. The circle indicates the electrode, and the three arrows indicated each of the Γ-X directions. (c) Electric-field distribution in the plane of the photonic crystal (left) and above the plane of the photonic crystal (right) calculated by 3D FDTD method. The large broken circle indicates the electrode area. The small circle represents the area where the corresponding interference pattern above the crystal becomes zero as indicated by the thick solid arrow. The square indicates the area where the corresponding interference pattern above the crystal is nonzero.

surface-emitting component must be calculated before the theoretical result can be compared directly to the results shown in Fig. 8(a). The surface-emitting component of the hexpole mode calculated using the 3D FDTD method, shown in Fig. 8(b), clearly agrees with the measured polarization pattern.

It is physically interesting that a polarization pattern on the scale of the lattice constant shown in Fig. 3(a), when emitted through the surface, leads to a similar pattern on the much larger length scale of the electrode. This can be examined in terms of the electric-field distribution. Figure 8(c) shows the electric-field distribution on (left) and above (right) the plane of the photonic crystal calculated by 3D FDTD method. Note that the right part of Fig. 8(c) is the same as Fig. 8(b) without the electrode shown. The large broken circle in the left figure indicates the electrode area. It can be seen in the left part of Fig. 8(c) that the field pattern resembles that of the Bloch wave shown in Fig. 3(a) for the area under electrode, however, the fields weaken or vanish outside the area of the electrode. The pattern observed above the photonic crystal plane loses the periodicity of the field pattern. The underlying physics of this phenomenon is thought to be interference of electromagnetic field patterns originating under the electrode leaking to the surface. For example, the amplitude of electric field in six equivalent directions is equal in the center area (small circle), as a result, corresponding interference pattern above the crystal becomes zero. Similarly, the amplitude of electric field in six equivalent directions is not equal at the boundary of the electrode
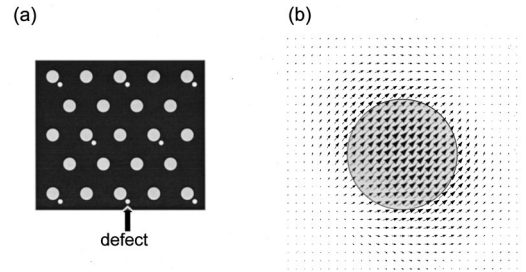

FIG. 9. (a) Schematic of defects introduced into 2D photonic crystal. (b) Electric-field pattern above the device calculated by 3D FDTD. The light gray area indicates the center of the device.

(square), resulting in a nonzero interference pattern in the field above the crystal. The crystal examined here clearly has a complicated polarization pattern, which in conjunction with the ring shape of the emission area, limit the range of potential applications. However, both these problems can be addressed by the introduction of defects into the photonic crystal structure, affording simple unidirectionally polarized emission with circular beam cross section.

From the above results, it is confirmed that the observed lasing oscillation really occurred at the band edge A. Observations of polarization patterns of other devices also suggested good correspondences between the lasing oscillation of other modes and the theoretical predictions.

C. Polarization control by defect engineering

The lasing observed here is unique to the 2D photonic crystal structure. However, the lasing modes have relatively complicated polarization patterns, affecting the range of application. These devices would be more readily applicable if the laser light were unidirectionally polarized. This can be achieved by introducing defects. Laser light from band edges A, B, C, or D is emitted in various polarization patterns depending on the field distribution in the plane of the 2D photonic crystal (see Fig. 3). The two degenerate modes of band edge D have the potential to exhibit unidirectional polarization if the modes can be excited separately. However, due to the degeneracy, these two bands are always excited simultaneously, and the resulting pattern is unpolarized. Therefore, by adding defects that eliminate the degeneracy, each split band of band edge D will yield a unidirectionally polarized emission. For example, we introduced defects into the 2D photonic crystal as shown in Fig. 9(a). Using one of the split bands of band edge D, the surface-emitting component of the electric field calculated by 3D FDTD is now unidirectionally and uniformly polarized at the center of the device, as shown in Fig. 9(b). In addition, the laser has a simple circular beam profile in contrast to the result shown in Fig. 8(c), which makes the device more readily applicable. The details of polarization control in the 2D photonic crystal cavity will be reported elsewhere.[13] From these results, we anticipate that by introducing an appropriate defect into the 2D photonic crystal, a laser with precisely controlled lasing mode and polarization direction over a large 2D area can be realized.
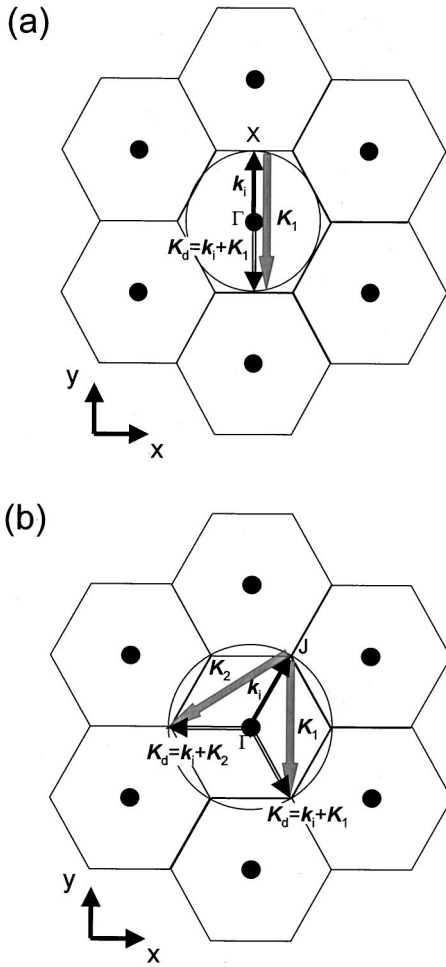
FIG. 10. Wave-vector diagram at (a) point I and (b) point II. k_i (solid line) and k_d (double line) indicate incident and diffracted wave vectors.
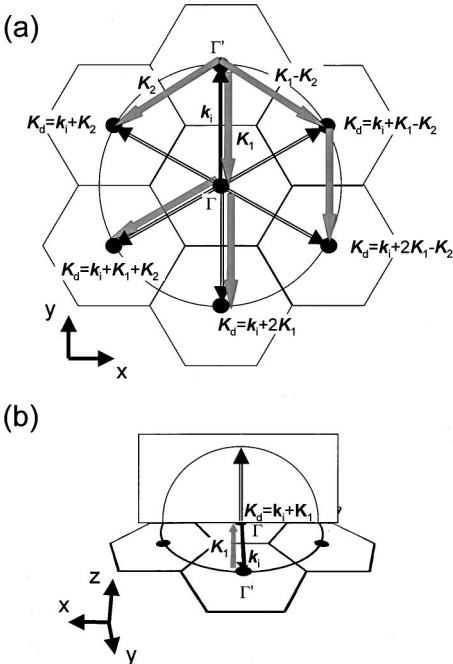

FIG. 11. Wave-vector diagram of (a) in-plane and (b) vertical directions at point III.
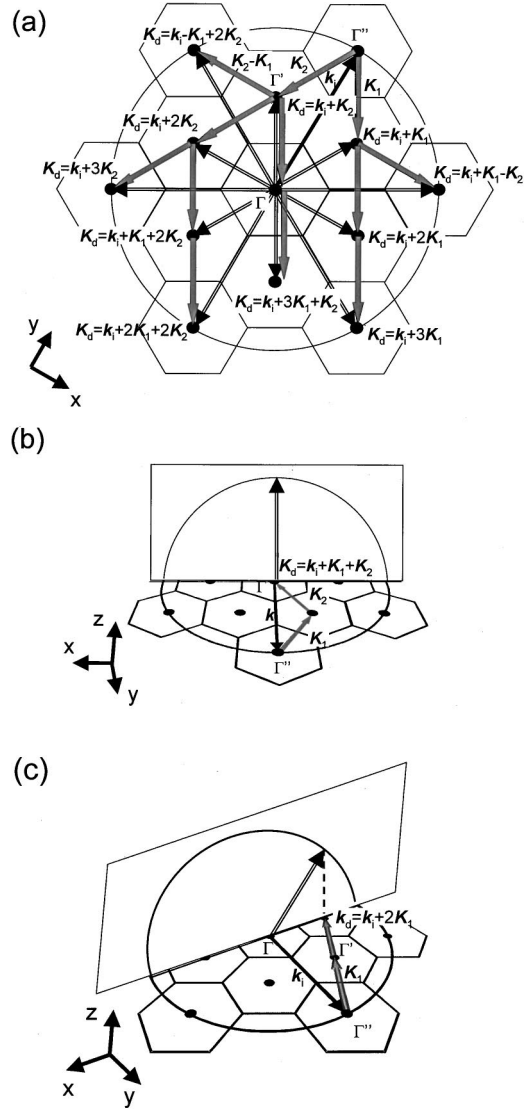

FIG. 12. Wave-vector diagram of (a) in-plane and (b) vertical directions at point IV. (c) Wave-vector diagram showing diffraction in an oblique direction at point IV.

This could lead to the fabrication of an unprecedented type of laser with superior features such as a high power, single mode, and large-area surface emission with a very narrow divergence angle and controlled polarization.

IV. CONCLUSION

We have theoretically investigated the band structure of the 2D photonic crystal laser and the electromagnetic field distributions of the possible lasing modes. The measurement of emission spectra over a large lasing area revealed that lasing occurs over the entire area at a single wavelength due to the multidimensional DFB effect, despite the large lasing area. The electric-field distributions (polarization characteristics) of the lasers were found to be in good agreement with the theoretical predictions, confirming the theoretically proposed model of lasing in 2D photonic crystal lasers. We have shown that the polarization patterns of the lasing modes can

be precisely controlled by introducing lattice defects into the photonic crystals. The 2D photonic crystal laser examined in this study represents an unprecedented type of laser with outstanding features.

APPENDIX: BRAGG DIFFRACTION IN 2D TRIANGULAR-LATTICE STRUCTURE

For simplicity, we consider a slab structure consisting of three layers. The 2D triangular-lattice structure is formed in the second layer. The reciprocal lattice of the structure is shown in Fig. 1(a). K_1 and K_2 are the Bragg grating vectors, with magnitude $|K| = 2\pi/a$, where a is the lattice constant. When we consider the Bragg diffraction of the TE mode lightwave in the structure, the incident lightwave and the diffracted lightwave satisfy the relationship,

$$k_d = k_i + q_1 K_1 + q_2 K_2, \quad (q_{1,2} = 0, \pm 1, \pm 2, \dots) \quad \text{(A1)}$$

$$\omega_d = \omega_i, \quad \text{(A2)}$$

where k_d, k_i, and q are the xy-component wave vectors of diffracted lightwaves, xy-component wave vectors of the incident lightwave, and order of coupling, respectively. In Eq. (A2) ω_d and ω_i are the frequency of diffracted and incident lightwaves, respectively. Equation (A1) represents the phase-matching condition, and Eq. (A2) represents the constant-frequency condition. First, we consider the Bragg diffraction of the lightwave at points I and II in Fig. 2(b). Figures 10(a) and 10(b) show the wave-vector diagrams at points I and II, respectively. The hexagonal regions are the tiled first Bril-louin zones of the structure. From Eq. (A2), the diffraction condition is satisfied when $|k_d|$ is equal to the diameter of the central circle. It can be clearly seen that the diffraction occurs only in the backward (180°) direction at point I, whereas diffraction occurs in two different Γ-J directions at point II, as shown in Fig. 10(b). Figure 11(a) shows the x-y plane at point III, at which the lightwave is diffracted in five different Γ-X directions; $k_i + K_1$ also reaches the Γ point. In this case, the incident lightwave is diffracted normal to the substrate surface because the Bragg condition is satisfied, as shown in Fig. 11(b). This is the same phenomenon that occurs in conventional grating-coupled surface-emitting lasers; the device, therefore, functions as a surface-emitting laser. Figures 12(a) and 12(b) show the in-plane and vertical diffraction at point IV. In this case, the lightwave is diffracted in five Γ-J directions and in the vertical direction similar to point III, and $k_i + q_1 K_1 + q_2 K_2$ reaches the six Γ' points. Figure 12(c) shows the wave-vector diagram of one Γ' point where the lightwave is diffracted in an oblique direction. The lightwave is also diffracted in a bottom oblique direction. The same diffraction phenomena occur at the other five Γ' points, resulting in diffraction in 19 directions at point IV.

*Email address: imada@kuee.kyoto-u.ac.jp

†Email address: snoda@kuee.kyoto-u.ac.jp

[1] H. Kogelnik and C. V. Shank, Appl. Phys. Lett. **18**, 152 (1971).

[2] I. P. Kaminov, H. P. Weber, and E. A. Chandross, Appl. Phys. Lett. **18**, 497 (1971).

[3] M. Imada, S. Noda, A. Chutinan, T. Tokuda, M. Murata, and G. Sasaki, Appl. Phys. Lett. **75**, 316 (1999).

[4] M. Meier, A. Mekis, A. Dodabalapur, A. Timko, R. E. Slusher, J. D. Joannopoulos, and O. Nalamasu, Appl. Phys. Lett. **74**, 7 (1999).

[5] K. Inoue, M. Sasada, J. Kawamata, K. Sakoda, and J. W. Haus, Jpn. J. Appl. Phys., Part 2 **38**, L157 (1999).

[6] M. Meier, A. Dodabalapur, J. A. Rogers, R. E. Slusher, A. Mekis, A. Timko, C. A. Murray, R. Ruel, and O. Nalamasu, J. Appl. Phys. **86**, 3502 (1999).

[7] M. Plihal and A. A. Maradudin, Phys. Rev. B **44**, 8565 (1991).

[8] M. Notomi, H. Suzuki, and T. Tamamura, Appl. Phys. Lett. **78**, 1325 (2001).

[9] S. Noda, K. Kojima, K. Mitsunaga, K. Kyuma, K. Hamanaka, and T. Nakayama, Appl. Phys. Lett. **51**, 1200 (1987).

[10] K. Sakoda, Phys. Rev. B **52**, 7982 (1995).

[11] K. S. Yee, IEEE Trans. Antennas Propag. **AP-14**, 302 (1966).

[12] G. Mur, IEEE Trans. Electromagn. Compat. **EMC-23**, 377 (1981).

[13] S. Noda, M. Yokoyama, M. Imada, A. Chutinan, and M. Mochizuki, Science **293**, 1123 (2001).